



# PRISM: Self-Pruning Intrinsic Selection Method for Training-Free Multimodal Data Selection

Jinhe Bi<sup>1,2,4</sup> Aniri<sup>1</sup> Danqi Yan<sup>1</sup> Yifan Wang<sup>1</sup> Wenke Huang<sup>3</sup>  
 Zengjie Jin<sup>1</sup> Xiaowen Ma<sup>1</sup> Sikuan Yan<sup>1</sup> Artur Hecker<sup>2</sup> Mang Ye<sup>3</sup>  
 Xun Xiao<sup>2\*</sup> Hinrich Schütze<sup>1,4</sup> Volker Tresp<sup>1,4</sup> Yunpu Ma<sup>1,4\*</sup>

<sup>1</sup> Ludwig Maximilian University of Munich <sup>2</sup> Munich Research Center, Huawei Technologies  
<sup>3</sup> School of Computer Science, Wuhan University <sup>4</sup> Munich Center for Machine Learning

## Abstract

Visual instruction tuning adapts pre-trained Multimodal Large Language Models (MLLMs) to follow human instructions for real-world applications. However, the rapid growth of these datasets introduces significant redundancy, leading to increased computational costs. Existing methods for selecting instruction data aim to prune this redundancy, but predominantly rely on computationally demanding techniques such as proxy-based inference or training-based metrics. Consequently, the substantial computational costs incurred by these selection processes often exacerbate the very efficiency bottlenecks they are intended to resolve, posing a significant challenge to the scalable and effective tuning of MLLMs. To address this challenge, we first identify a critical, yet previously overlooked, factor: the anisotropy inherent in visual feature distributions. We find that this anisotropy induces a *Global Semantic Drift*, and overlooking this phenomenon is a key factor limiting the efficiency of current data selection methods. Motivated by this insight, we devise **PRISM**, the first training-free framework for efficient visual instruction selection. PRISM surgically removes the corrupting influence of global background features by modeling the intrinsic visual semantics via implicit re-centering. Empirically, PRISM reduces the end-to-end time for data selection and model tuning to just 30% of conventional pipelines. More remarkably, it achieves this efficiency while simultaneously enhancing performance, surpassing models fine-tuned on the full dataset across eight multimodal and three language understanding benchmarks, culminating in a 101.7% relative improvement over the baseline. The code is available for access via [this repository](#).

## 1 Introduction

The advent of MLLMs marks a significant milestone in artificial intelligence, endowing models

\*Corresponding authors: [cognitive.yunpu@gmail.com](mailto:cognitive.yunpu@gmail.com), [drxiaoxun@gmail.com](mailto:drxiaoxun@gmail.com).

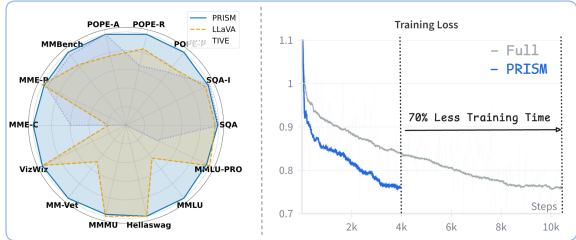


Figure 1: **PRISM achieves state-of-the-art performance with substantially greater training efficiency.** **(Left)** On a suite of multimodal and language benchmarks, PRISM (blue) uniformly outperforms strong baselines like LLaVA-665K and TIVE. **(Right)** The training loss curve demonstrates that PRISM converges faster and to a lower loss, reducing training time by 70% compared to the LLaVA baseline.

with remarkable capabilities to process and reason over interleaved visual and textual information (Liu et al., 2024a; Zhu et al., 2023; Dai et al., 2023). The standard paradigm for building these models is a two-stage process: (1) large-scale pre-training on web-scraped image-text pairs to establish foundational cross-modal alignment, followed by (2) visual instruction tuning to hone the model’s ability to follow complex, task-oriented instructions. While instruction tuning is critical for unlocking state-of-the-art performance, its effectiveness is increasingly challenged by the data it relies on. Publicly curated datasets are expanding exponentially but are often saturated with low-quality and redundant examples (Chen et al., 2024; Wei et al., 2023). Naively training on this noisy data inflates computational costs and, paradoxically, can degrade final model performance. This predicament has created an urgent need for efficient visual instruction selection methods that can identify a compact, high-quality subset of data.

Existing selection strategies predominantly fall into two categories. The first, **Proxy-Based Selection**, employs external models such as specialized scorers (Chen et al., 2024) or auxiliary MLLMs (Lee et al., 2024) to estimate the importance of

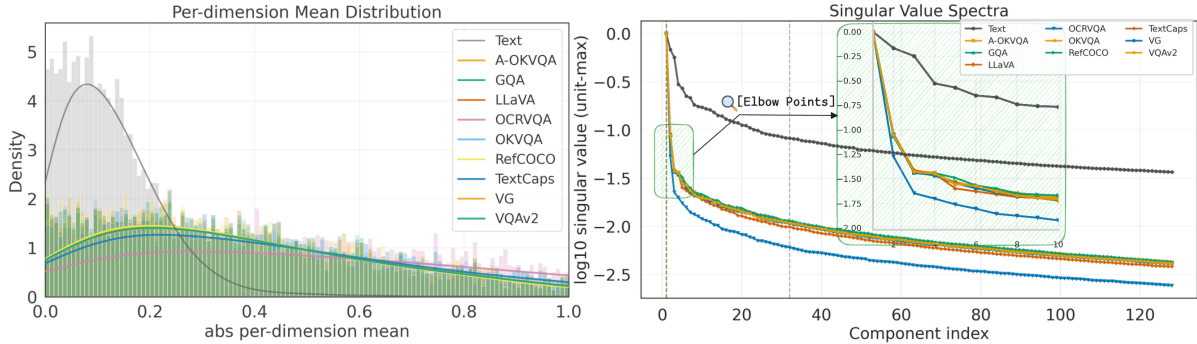


Figure 2: **Visual Diagnosis of Representation Anisotropy in Pre-trained MLLM Features.** **(Left)** The per-dimension mean distribution reveals a fundamental disparity: unlike text features (grey) which are well-centered around zero, all visual instruction datasets exhibit a significant non-zero mean. This provides direct evidence that visual embeddings occupy a biased, narrow cone, which is the geometric origin of *Global Semantic Drift*. **(Right)** The singular value scree plot confirms this diagnosis. The sharp “elbow point” indicates that the feature variance is confined to a few dominant dimensions—a classic symptom of representation degeneration. Detailed statistics and qualitative case studies are provided in Appendix G and Fig. 8.

each data point. This approach, however, introduces substantial computational overhead from the proxy model’s training and inference demands and is susceptible to selection bias when its objectives or architecture misalign with the target model. The second category, **Training-Based Selection**, leverages signals from the target model’s own training dynamics, using metrics based on training loss (Liu et al., 2024d) or influence functions (Wu et al., 2025). While this avoids proxy misalignment, these methods are often prohibitively expensive, requiring iterative gradient computations that can be as costly as training on the full dataset itself.

A critical limitation unites both paradigms: their substantial computational costs often negate the intended efficiency gains and can even lead to performance degradation under practical resource constraints. This reveals a fundamental gap in the current landscape—the lack of a selection method that is both effective at identifying high-quality data and genuinely efficient to deploy. In this work, we argue that the key to bridging this gap lies not in designing more complex selection architectures, but in diagnosing and correcting a fundamental flaw within the MLLM’s own visual representations. Our investigation begins with an analysis of the pre-trained visual feature distribution, where we uncover a critical, yet previously overlooked, property: *representation anisotropy*.

As illustrated in Figure 2, we first observe that unlike text features, the mean embedding vector of visual features across diverse datasets is consistently non-zero. This signifies that the representations are confined to a narrow cone in high-dimensional space, a geometric bias that systemati-

cally distorts common similarity metrics (Levi and Gilboa, 2024). This distortion gives rise to a phenomenon we term *Global Semantic Drift*, where global background context from different visual domains misleadingly inflates cosine similarity scores. A deeper analysis of the feature distribution’s singular values confirms this profound anisotropy, a classic indicator of representation degeneration (Gu et al., 2019). We posit that this anisotropy masks the intrinsic capability of the pre-trained features to discern data redundancy, as in such a space, geometric distance is no longer a faithful proxy for semantic similarity. We argue that the failure of prior methods to account for this anisotropy is a primary source of their excessive data selection overhead. Therefore, to effectively measure data redundancy, it is essential to first re-center the feature distribution to mitigate this anisotropic bias and reveal the underlying semantic structure.

Building on this insight, we introduce **PRISM**, a novel, training-free framework that redefines multimodal data selection. PRISM bypasses the complexities of existing proxy-based and training-based methods by establishing a third paradigm we term **Intrinsic Selection**. The philosophy of this paradigm is to unlock the latent potential of an MLLM’s pre-trained representations by correcting, rather than circumventing, the flawed geometry of its feature space. At its core, PRISM counteracts representation anisotropy by performing an *implicit re-centering* of the visual feature distribution. It effectively nullifies the global, non-semantic shift in the raw embeddings. This re-centering restores a well-behaved isotropic geometry to the feature space. Crucially, it is this restoration that allows

the **intrinsic features** themselves to become a direct and reliable signal for identifying visual semantic redundancy. With the geometric distortions removed, there is no need for external models or expensive gradient computations, enabling highly effective visual instruction selection with negligible computational cost.

We validate PRISM through extensive experiments on a diverse set of multimodal benchmarks, evaluating its efficacy against state-of-the-art selection methods. Our results demonstrate that an MLLM fine-tuned on a small, PRISM-selected dataset (PRISM-Instruct-250K) outperforms models trained on the full dataset while reducing training time by 70%. Furthermore, we conduct analyses on *Cross-Model Generalization* and *Knowledge Retention*, demonstrating that PRISM generalizes effectively across different MLLM architectures and better preserves the model’s linguistic capabilities compared to full-dataset training.

#### Our key contributions are as follows:

- We identify *representation anisotropy* in the visual features of MLLMs as the root cause of inefficient data selection and diagnose its primary symptom, a *Global Semantic Drift*, which distorts similarity metrics.
- We propose **PRISM**, a training-free framework that establishes a new **Intrinsic Selection** paradigm. By performing an *implicit re-centering* of visual features, PRISM restores an isotropic geometry, unlocking the MLLM’s own features for redundancy detection.
- Our experiments show PRISM sets a new state-of-the-art, reducing training time by 70% while yielding performance superior to models fine-tuned on the complete dataset.

## 2 Visual Instruction Selection

While numerous methods exist for visual instruction selection, a rigorous framework for evaluating their practical utility is often overlooked. Here we establish two fundamental principles that any effective selection strategy must satisfy to be considered viable in real-world applications. These principles serve as the foundation for a new quantitative metric to holistically assess selection efficacy.

#### Principle 1: Performance Fidelity

A selected data subset must yield model performance equal to or greater than that achieved with the full dataset.

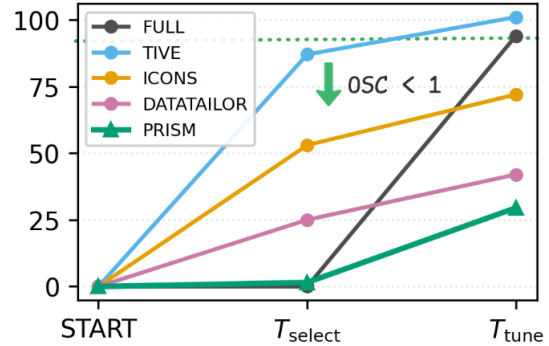


Figure 3: End-to-end computational cost (GPU Hours) vs. final model performance. PRISM achieves state-of-the-art performance while significantly reducing total time, thus satisfying the condition  $OSC < 1$ .

#### Principle 2: Net Efficiency Gain

The total time consumed by data selection and subsequent model tuning must be strictly less than the time required for tuning on the full dataset.

To unify these principles into a single, quantifiable measure, we introduce the **Overall Selection Cost (OSC)** score. This metric captures the total overhead of a selection method in terms of both performance and computation. Formally, let  $\mathcal{D}_{full}$  be the full instruction tuning dataset and  $\mathcal{D}_{sub}$  be the selected subset. Let  $P(\mathcal{D})$  denote the final performance score on the downstream benchmark achieved by a model fine-tuned on a dataset  $\mathcal{D}$ . The fine-tuning time on the full dataset is  $T_{tune}(\mathcal{D}_{full})$ , while the total time for a selection pipeline is the sum of the selection time  $T_{select}$  and the subset fine-tuning time  $T_{tune}(\mathcal{D}_{sub})$ . The Overall Selection Cost (OSC) score,  $\mathcal{C}$ , is defined as:

$$\mathcal{C} = \underbrace{\left( \frac{P(\mathcal{D}_{full})}{P(\mathcal{D}_{sub})} \right)}_{\text{Performance Ratio}} \times \underbrace{\left( \frac{T_{select} + T_{tune}(\mathcal{D}_{sub})}{T_{tune}(\mathcal{D}_{full})} \right)}_{\text{Time Ratio}}. \quad (1)$$

A selection method is considered practically viable if and only if its OSC score  $\mathcal{C} < 1$ . This single criterion guarantees that any computational savings are not achieved at the expense of final model performance, thus certifying a true net gain in efficiency as shown in Fig. 3.

As illustrated in Fig. 4, existing visual instruction selection methods can be broadly categorized into two main paradigms. The first is **Proxy-Based Selection**, where the target MLLM remains a black box, and data quality is evaluated using an external

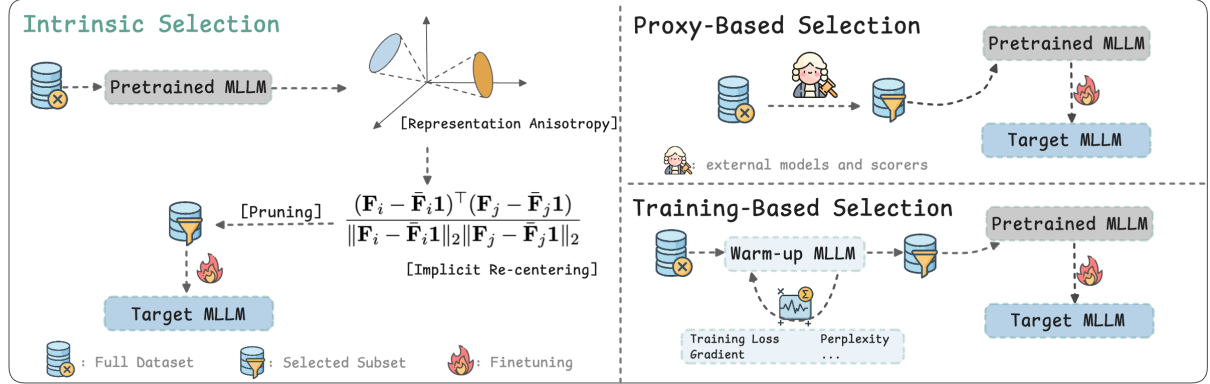


Figure 4: **A Comparison of Data Selection Paradigms.** Existing methods, such as Proxy-Based and Training-Based Selection, introduce significant computational overhead by relying on external scorers or expensive, iterative training loops to estimate data importance. In contrast, our proposed **Intrinsic Selection** paradigm operates on a more fundamental principle: we first diagnose a geometric flaw—*representation anisotropy*—in the MLLM’s native visual features. We then apply an *implicit re-centering* to correct this bias. This isotropic restoration unlocks the intrinsic semantic structure of the data, enabling highly effective and training-free pruning in a single pass.

scoring function. This function can be a purpose-built scoring model (Chen et al., 2024), a human reward model, or a powerful LLM-based scorer (Wei et al., 2023). Some approaches also train a smaller proxy MLLM to guide the data selection for a larger target model (Lee et al., 2024). The second category is **Training-Based Selection**. In this approach, the target MLLM is actively used to assess data value by computing metrics derived from its training dynamics, such as training loss, perplexity, or gradient information on a given data partition. Yet both paradigms exhibit structural drawbacks: they risk **performance degradation**, incur **high computational costs**, and introduce **Proxy-Based bias**. A fuller discussion appears in Appendix E. We contend that these drawbacks share a single, underappreciated root cause: the overlooked *representation anisotropy* inherent in MLLM visual feature distributions. To address this geometric pathology, we introduce **PRISM**—a self-PRuning Intrinsic Selection Method—that enables training-free multimodal data selection by operating directly on the model’s intrinsic, re-centered features.

### 3 PRISM

#### 3.1 Representation Anisotropy

To reveal the potential of pre-trained intrinsic features, we first investigate the feature distribution and uncover a critical, yet previously overlooked property in previous data selection methods: representation anisotropy. Representation anisotropy is a geometric pathology observed in many high-dimensional embedding spaces (Levi and Gilboa, 2024; Zhang et al., 2020). In an *isotropic* embed-

ding, vectors are uniformly distributed around the origin and exhibit equal variance along every dimension; mathematically, the covariance matrix of an isotropic set is proportional to the identity. Such a space fully exploits its dimensionality and provides maximal directional diversity for encoding semantic concepts. As illustrated in Figure 2, we begin with a deep analysis of the feature geometry from a pre-trained MLLM, revealing a critical flaw in its visual representations. We find a stark disparity between modalities: while textual features are well-centered around a zero mean, the feature distributions for all visual datasets exhibit a significant, non-zero mean. This confirms that visual embeddings are confined to a narrow cone in high-dimensional space—a geometric bias that systematically distorts similarity metrics and gives rise to a phenomenon we term *Global Semantic Drift*, where shared background context is misinterpreted as semantic content. A singular value analysis of these distributions further confirms this profound anisotropy. The sharp “elbow point” observed in Figure 2 (right) indicates that feature variance is concentrated in only a few dominant dimensions, a classic symptom of representation degeneration that corrupts semantic distance measures (Gu et al., 2019; Levi and Gilboa, 2024). We posit that this unaddressed anisotropy is the primary reason for the inefficiency of prior art.

#### 3.2 Theoretical Analysis: Anisotropy as a Source of Computational Overhead

To formalize this, let  $\phi : \mathcal{D} \rightarrow \mathbb{R}^d$  be an embedding function mapping data points to representation vectors. The observed anisotropy implies a non-zero

mean vector  $\mu = \mathbb{E}[\phi(d)]$  with significant magnitude. We can thus decompose any representation  $\mathbf{x}_i = \phi(d_i)$  into a shared global component and a sample-specific residual:

$$\mathbf{x}_i = \mu + \delta_i \quad (2)$$

where  $\delta_i$  encodes the unique semantics of sample  $d_i$ . The defining characteristic of anisotropy is that the shared component dominates, i.e.,  $\|\mu\|_2 \gg \mathbb{E}[\|\delta_i\|_2]$ . This geometric property has a catastrophic consequence for standard metrics.

**Theorem 1.** *In an anisotropic representation space where  $\|\mu\|_2 \gg \mathbb{E}[\|\delta_i\|_2]$ , the cosine similarity between any two randomly sampled vectors  $\mathbf{x}_i$  and  $\mathbf{x}_j$  is dominated by the global drift  $\mu$ , masking their semantic dissimilarity encoded in  $\delta_i, \delta_j$ .*

*Proof.* The cosine similarity is given by:

$$\cos(\mathbf{x}_i, \mathbf{x}_j) = \frac{(\mu + \delta_i)^\top (\mu + \delta_j)}{\|\mu + \delta_i\|_2 \|\mu + \delta_j\|_2} \quad (3)$$

The numerator expands to  $\|\mu\|_2^2 + \mu^\top (\delta_i + \delta_j) + \delta_i^\top \delta_j$ . The denominator can be approximated using a first-order Taylor expansion  $\sqrt{a+b} \approx \sqrt{a} + \frac{b}{2\sqrt{a}}$  for small  $b$ . As  $\|\mu\|_2$  is the dominant term, we have  $\|\mu + \delta_i\|_2 \approx \|\mu\|_2 + \frac{\mu^\top \delta_i}{\|\mu\|_2}$ . Substituting these into the main equation and retaining only the dominant terms yields:

$$\begin{aligned} \cos(\mathbf{x}_i, \mathbf{x}_j) &\approx \frac{\|\mu\|_2^2}{\left(\|\mu\|_2 + \frac{\mu^\top \delta_i}{\|\mu\|_2}\right) \left(\|\mu\|_2 + \frac{\mu^\top \delta_j}{\|\mu\|_2}\right)} \\ &\approx 1 - \frac{1}{2} \left\| \frac{\delta'_i}{\|\mu\|_2} - \frac{\delta'_j}{\|\mu\|_2} \right\|_2^2 \approx 1 \end{aligned} \quad (4)$$

where  $\delta'$  is the component of  $\delta$  orthogonal to  $\mu$ . The true semantic similarity, proportional to  $\delta_i^\top \delta_j$ , is relegated to lower-order terms, rendering the metric ineffective for distinguishing unique samples. A full derivation is provided in Appendix F.  $\square$

**Corollary 2.** *Due to Theorem 1, computationally efficient data selection algorithms predicated on geometric dissimilarity in the raw embedding space (e.g., Farthest-Point Sampling, distance-based clustering) fail to select semantically diverse subsets.*

This failure of inexpensive geometric proxies forces existing methods to adopt computationally intensive strategies to approximate the true, underlying data value, effectively paying a high computational “tax” for ignoring the geometric flaw of the space.

### 3.3 Redundancy Identification via Implicit Re-centering of Intrinsic Features

To solve the Representation Anisotropy and alleviate Global Semantic Drift, PRISM employs a implicit re-centering operation to restore a well-behaved isotropic geometry to the feature space. Crucially, it is this restoration that allows the intrinsic features themselves to become a direct and reliable signal for identifying semantic redundancy.

Let our dataset be  $\mathcal{D} = \{d_1, \dots, d_N\}$ . For each data point  $d_i$ , we first extract a high-level feature representation  $\mathbf{F}_i \in \mathbb{R}^d$  from an intermediate layer of pretrained MLLM. The set of these vectors,  $\{\mathbf{F}_i\}_{i=1}^N$ , forms the anisotropic space diagnosed in Section 3.2, characterized by the non-zero global mean vector  $\mu_{\mathcal{F}} = \frac{1}{N} \sum_{i=1}^N \mathbf{F}_i$ . To measure similarity in a geometrically corrected space where the influence of this global drift is nullified. We achieve this through an *implicit re-centering* operation embedded within the Pearson correlation coefficient. Let  $\bar{\mathbf{F}}_i \in \mathbb{R}$  be the scalar mean of the elements within a single vector  $\mathbf{F}_i$ . We define the centered vector as  $\mathbf{F}'_i = \mathbf{F}_i - \bar{\mathbf{F}}_i \mathbf{1}$ , where  $\mathbf{1}$  is a vector of ones.

$$\rho(\mathbf{F}_i, \mathbf{F}_j) = \frac{(\mathbf{F}_i - \bar{\mathbf{F}}_i \mathbf{1})^\top (\mathbf{F}_j - \bar{\mathbf{F}}_j \mathbf{1})}{\|\mathbf{F}_i - \bar{\mathbf{F}}_i \mathbf{1}\|_2 \|\mathbf{F}_j - \bar{\mathbf{F}}_j \mathbf{1}\|_2} \quad (5)$$

This operation measures the alignment of two vectors’ internal variation patterns, making it invariant to the kind of global, location-based shifts that characterize anisotropy. By operating on these centered vectors  $\mathbf{F}'_i$ , we effectively evaluate the relationship between the unique semantic components,  $\delta_i$ , that our theory identified.

With a robust similarity metric established, we quantify the redundancy of each sample. A sample is considered redundant if its unique semantic information is highly correlated with many other samples in the dataset. We define the *Redundancy Score*  $\mathcal{R}(d_i)$  for a sample  $d_i$  as its expected correlation with the rest of the corpus:

$$\mathcal{R}(d_i) = \frac{1}{N-1} \sum_{j=1, j \neq i}^N \rho(\mathbf{F}_i, \mathbf{F}_j) \quad (6)$$

A low score  $\mathcal{R}(d_i)$  indicates that the sample is a semantic outlier, contributing novel information to the dataset. Conversely, a high score signifies high conformity and thus redundancy. The final selection process aims to construct a subset  $\mathcal{D}_{\text{select}}$  that is minimally redundant. Given a selection budget

---

**Algorithm 1** PRISM

---

```
1: Input: Dataset  $\mathcal{D} = \{d_1, \dots, d_N\}$ , MLLM
   components (VE, Proj,  $\text{LLM}^{(l)}$ ), percentile  $\tau$ 
2: Output: Selected subset  $\mathcal{D}_{\text{select}}$ 
3: Anisotropic Feature Extraction:
4: for all  $d_i = (I_i, T_i) \in \mathcal{D}$  do
5:    $v_i \leftarrow \text{VE}(I_i)$ 
6:    $z_i \leftarrow \text{Proj}(v_i)$ 
7:    $\mathbf{F}_i \leftarrow \frac{1}{T} \sum_{t=1}^T \text{LLM}^{(l)}(z_i)_t$  /* Obtain
   layer- $l$  representation */
8: end for
9: Redundancy Identification via Implicit Re-
   centering:
10: for all  $i \in \{1, \dots, N\}$  do
11:   Let  $\bar{F}_k$  be the scalar mean of the elements
   in vector  $\mathbf{F}_k$ .
12:    $\mathcal{R}_i \leftarrow \frac{1}{N-1} \sum_{j \neq i} \frac{(\mathbf{F}_i - \bar{F}_k \mathbf{1})^\top (\mathbf{F}_j - \bar{F}_k \mathbf{1})}{\|\mathbf{F}_i - \bar{F}_k \mathbf{1}\|_2 \|\mathbf{F}_j - \bar{F}_k \mathbf{1}\|_2}$  /* Score
   redundancy in the corrected space */
13: end for
14: Diversity-Aware Pruning:
15:  $q_\tau \leftarrow \text{Percentile}(\{\mathcal{R}_k\}_{k=1}^N, \tau)$  /* Find score
   threshold at  $\tau$ -th percentile */
16:  $\mathcal{D}_{\text{select}} \leftarrow \{d_i \in \mathcal{D} \mid \mathcal{R}_i \leq q_\tau\}$  /* Filter
   samples with low redundancy scores */
17: return  $\mathcal{D}_{\text{select}}$ 
```

---

defined by a percentile threshold  $\tau$ , we select all samples whose redundancy scores fall below the  $\tau$ -th percentile of the score distribution:

$$\mathcal{D}_{\text{select}} = \{d_i \in \mathcal{D} \mid \mathcal{R}(d_i) \leq Q_\tau(\{\mathcal{R}(d_k)\}_{k=1}^N)\}, \quad (7)$$

where  $Q_\tau(\cdot)$  is the function that computes the  $\tau$ -th percentile. This principled approach ensures that the selected subset is enriched with semantically diverse and informative samples, having explicitly corrected for the geometric distortions of the original embedding space.

## 4 Experiments

### 4.1 Experiment Setup

**Dataset & Model:** We evaluate PRISM on the visual instruction tuning dataset LLaVA-665K (Liu et al., 2024a), using LLaVA-1.5-7B (Liu et al., 2024a) as our primary base model. All experiments are conducted for one epoch following the official fine-tuning hyperparameters. To ensure a fair comparison, we maintain a consistent training environment across all evaluations.

**Baselines:** We compare PRISM against a comprehensive set of baselines, including Random Se-

lection, Instruction Length, Perplexity (Liu et al., 2024d), GraNd (Paul et al., 2023), EL2N (Paul et al., 2023), InstructionGPT-4 (Wei et al., 2023), SELF-FILTER (Chen et al., 2024), TIVE (Liu et al., 2024d), COINCIDE (Lee et al., 2024), DataTailor (Yu et al., 2024a), and ICONS (Wu et al., 2025). To ensure fair comparisons, we adopt the experimental settings and incorporate results from ICONS (Wu et al., 2025) and TIVE (Liu et al., 2024d).

**Benchmarks.** Following the rigorous framework of LLaVA-1.5 (Liu et al., 2024a), we evaluate PRISM across a comprehensive suite of seven diverse benchmarks. This suite is designed to probe a wide array of MLLM capabilities, including fine-grained perception, visual reasoning, hallucination detection, and complex conversational skills. Our evaluation includes MMBench (Liu et al., 2024c), ScienceQA (Lu et al., 2022), MME (Yin et al., 2023), POPE (Li et al., 2023), VizWiz (Gurari et al., 2018), MM-Vet (Yu et al., 2024b), and MMMU (Yue et al., 2024). Detailed descriptions of each benchmark are provided in Appendix H.

### 4.2 Main Results

We present a comprehensive evaluation to validate PRISM’s effectiveness and robustness. Our primary results in Table 1 demonstrate that PRISM outperforms both full-dataset fine-tuning and state-of-the-art selection methods on the LLaVA-1.5-7B model. We then showcase PRISM’s broad applicability by demonstrating its strong performance across different MLLM architectures (Table 6) and in uni-modal, text-only settings (Table 2). We highlight two key findings:

**State-of-the-Art Performance with Less Data.** As shown in Table 1, PRISM achieves superior performance across all benchmarks, outperforming full-dataset fine-tuning by a relative **1.7%**. The gains are particularly notable on complex reasoning tasks like MMBench (65.2 vs. 64.3) and MM-Vet (32.0 vs. 31.1). This demonstrates that PRISM preferentially selects high-value, instruction-rich data that existing methods.

**Effective Hallucination Mitigation.** PRISM sets a new state-of-the-art on all POPE subsets for hallucination detection, surpassing even specialized methods like ICONS. This result suggests that our core mechanism—alleviating representation anisotropy via implicit re-centering—is highly effective at removing samples containing spurious semantic drift, which are a known cause of object hallucination.

**Balanced Efficiency and Performance.** As il-

Method	SQA	SQA-I	VizWiz	POPE-P	POPE-R	POPE-A	MM-Vet	MMBench	MME-P	MME-C	MMMU	Rel. (%)
Full-Finetune	69.4	66.8	50.0	86.1	87.3	84.2	31.1	64.3	1510.7	311.9	35.4	100%
Random	65.5	64.5	48.1	85.1	84.6	83.6	30.2	55.5	1492.0	233.5	30.5	93.2%
Length	66.8	66.7	47.0	85.4	85.5	84.1	31.5	57.0	1422.1	306.0	33.1	96.6%
EL2N	70.2	70.6	44.4	85.6	85.6	85.6	-	61.6	1356.5	294.7	-	97.2%
Perplexity	70.5	67.9	-	83.3	83.3	83.3	-	62.3	1393.3	260.7	-	95.8%
GraNd	71.4	68.4	37.8	82.5	82.5	82.5	-	62.9	1400.5	287.1	-	94.6%
TIVE	72.2	70.6	-	85.6	85.6	85.6	-	63.2	1433.0	322.1	-	100.6%
InstructionGPT-4	-	-	-	-	-	-	31.4	463.3	-	-	-	39.75%
Self-Filter	-	61.4	53.2	83.8	83.8	83.8	-	61.4	1306.2	-	-	96.1%
COINCIDE	-	69.2	46.8	86.1	86.1	86.1	-	63.1	1495.6	-	-	99.3%
ICONS	-	70.8	-	87.5	87.5	87.5	-	63.1	1485.7	-	-	101.0%
DataTailor	71.0	-	49.5	85.3	85.3	85.3	-	-	1476.1	319.2	-	99.9%
PRISM (Ours)	<b>71.3</b>	<b>69.1</b>	<b>50.1</b>	<b>87.7</b>	<b>88.7</b>	<b>85.5</b>	<b>32.0</b>	<b>65.2</b>	1470.0	<b>330.0</b>	34.7	<b>101.7%</b>

Table 1: Evaluation of PRISM against full fine-tuning and existing data selection approaches across multiple multimodal understanding benchmarks. PRISM achieves superior performance, surpassing full fine-tuning while significantly reducing computational costs. Metrics in **bold** indicate improvements over the full fine-tuning baseline. For POPE, we report the average score across three subsets for certain baselines due to the unavailability.

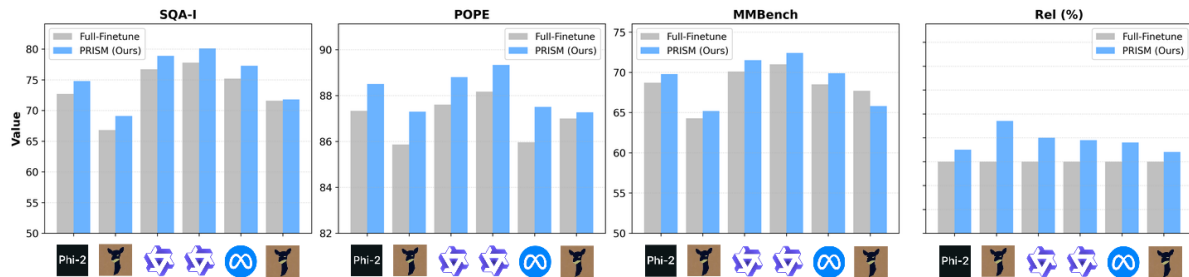


Figure 5: **Generalization across diverse MLLM families and scales.** Comparison of PRISM (blue) and full fine-tuning (grey) across SQA-I, POPE, MMBench, and Rel. (%) (detailed numerical results provided in Table 6). Results for **Phi-2**, **Vicuna**, **Llama-3**, and **Qwen2.5** confirm that PRISM’s performance gains are architecture-agnostic and transfer robustly across varied backbones and vision encoders.

lustrated in Figure 3, PRISM strikes an optimal balance between computational cost and model performance. While strong Training-Based methods like TIVE can achieve comparable performance (100.6% rel.), their substantial selection overhead often causes the total end-to-end time to exceed that of full fine-tuning, violating our Principle of Net Efficiency Gain. In stark contrast, PRISM not only achieves superior accuracy (**101.7%** rel.) but also reduces the total pipeline time by approximately **70%**. This exceptional efficiency is inherent to our training-free design, where feature extraction and correlation computations are performed in a single offline pass with negligible overhead compared to iterative training. A detailed breakdown of the wall-clock runtime can be found in Appendix K.

### 4.3 In-Depth Model Behavior Analysis

**Cross-Model Generalization and Scalability.** PRISM’s selection mechanism generalizes robustly across diverse MLLM architectures by correcting representation anisotropy. By identifying semantically dense samples, we establish the approach’s

Model	Hellaswag	MMLU	MMLU-PRO	Rel. (%)
LLaVA-Phi-2-3B	66.0	50.5	9.1	100%
PRISM-3B	<b>67.4</b>	<b>52.7</b>	8.6	<b>100.3%</b>
LLaVA-Vicuna-7B	66.5	35.0	17.8	100%
PRISM-7B	<b>66.5</b>	<b>41.1</b>	15.7	<b>101.9%</b>
LLaVA-Vicuna-13B	69.5	36.2	6.8	100%
PRISM-13B	<b>69.6</b>	<b>39.5</b>	<b>12.4</b>	<b>130.6%</b>

Table 2: PRISM effectively mitigates the knowledge forgetting problem commonly associated with visual instruction tuning.

breadth across five model–encoder combinations. Results demonstrate that effectiveness holds for both small and large language models—including Vicuna, Phi-2, Qwen2.5, and Llama-3—and for distinct vision encoders like CLIP and SigLIP (details in Appendix 5). These findings, illustrated in Fig. 5, confirm that PRISM’s gains are not specific to the LLaVA architecture but transfer effectively across diverse multimodal families.

**Language Knowledge Retention.** Visual instruction tuning is known to degrade a model’s foundational language capabilities, a phenomenon often

Method	SQA	SQA-I	VizWiz	POPE-P	POPE-R	POPE-A	MM-Vet	MMBench	MME-P	MME-C	MMU	Rel. (%)
Deep Layer	71.2	69.1	51.6	86.6	88.0	84.2	31.1	62.9	1477.0	254.0	34.5	97.2%
Middle Layer	70.9	69.1	47.7	86.5	87.8	84.2	31.9	65.0	1517.1	276.0	34.9	97.9%
✓ Shallow Layer	<b>71.3</b>	<b>69.1</b>	50.1	<b>87.7</b>	<b>88.7</b>	<b>85.5</b>	<b>32.0</b>	<b>65.2</b>	1470.0	<b>330.0</b>	34.7	<b>100.0%</b>
High Correlation	70.6	68.0	48.1	85.8	87.6	83.9	30.7	64.0	1428.5	275.3	33.5	96.3%
Moderate Correlation	71.0	69.7	48.3	85.9	86.7	84.0	30.0	64.2	1509.0	286.0	34.1	97.3%
✓ Low Correlation	<b>71.3</b>	69.1	<b>50.1</b>	<b>87.7</b>	<b>88.7</b>	<b>85.5</b>	<b>32.0</b>	<b>65.2</b>	1470.0	<b>330.0</b>	<b>34.7</b>	<b>100.0%</b>
Last Token	69.9	67.3	49.4	87.4	88.3	85.0	31.6	62.6	1471.0	272.0	35.3	97.4%
✓ Avg Pooling	<b>71.3</b>	<b>69.1</b>	<b>50.1</b>	<b>87.7</b>	<b>88.7</b>	<b>85.5</b>	<b>32.0</b>	<b>65.2</b>	1470.0	<b>330.0</b>	34.7	<b>100.0%</b>

Table 3: **Ablation study validating the core design principles of PRISM.** The results confirm that performance is maximized by using Shallow Layer features (preserving a cleaner geometric structure), selecting for Low Correlation (maximizing informational diversity), and applying Average Pooling (ensuring a holistic representation).

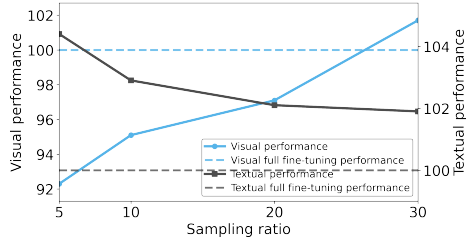


Figure 6: **Performance trade-off as a function of PRISM’s sampling ratio.** Visual performance (blue) improves with more data, while textual performance (grey) is best preserved with smaller subsets.

termed "knowledge forgetting" (Zhang et al., 2024). We show that PRISM not only mitigates this effect but can even enhance text-only performance. We hypothesize this is because PRISM’s correlation-based pruning effectively removes samples with spurious visual-textual associations. By filtering out this "noisy" data that often causes catastrophic forgetting, our method provides a cleaner training signal. As demonstrated in Table 2 on language-centric benchmarks (MMLU, MMLU-PRO, and HellaSwag), models trained on the PRISM subset consistently outperform their full-dataset-trained counterparts. This highlights a dual benefit of PRISM: achieving state-of-the-art multimodal performance without sacrificing language competency.

#### 4.4 Analysis of the Sampling Ratio

We analyze PRISM’s performance across different sampling ratios to understand the trade-off between the data budget and dual-modality capabilities (Figure 6). The results reveal a highly favorable and predictable trade-off: visual performance scales with the subset size, surpassing the full-dataset baseline with just 30% of the data. More strikingly, smaller subsets are optimal for mitigating catastrophic forgetting, with textual performance peaking at the 5% ratio. This confirms that PRISM’s core mechanism excels at pruning noisy data that degrades foundational language skills, offering robust performance across all data budgets.

#### 4.5 Ablation Study

To validate the core design choices of PRISM, we conduct systematic ablation studies on three key components: the source of visual features, the correlation-based scoring, and the token aggregation strategy.

**Influence of LLM Layer Selection.** We find that features from a **Shallow Layer** (Layer 1) are most effective for PRISM, significantly outperforming those from middle or deep layers (Table 3). This suggests that the fundamental geometric properties required for redundancy detection are most distinct in early layers, before complex abstractions introduce further representational artifacts.

**Impact of Correlation-based Selection.** Validating our central hypothesis, we show that selecting the **Low-Correlation** data subset yields the highest performance. This confirms that our implicit re-centering strategy effectively identifies informational diversity and prunes redundant samples that provide diminishing returns for model training (see Appendix E for further analysis).

**Effect of Token Aggregation Strategy.** We confirm that using an **Average** of all image tokens to form the global feature vector is superior to using only the **Last Image Token**. Averaging provides a more holistic and robust representation of an image’s semantics, which is crucial for the stability of our geometric analysis, whereas relying on a single token can be susceptible to positional biases.

### 5 Conclusion

We trace MLLM selection inefficiency to representation anisotropy and propose **PRISM**, a training-free method that restores semantic structure via implicit re-centering. Empirically, **PRISM** reduces training time by 70% while surpassing full-dataset performance, advocating for a shift toward geometry-aware curation over complex heuristics.

## Limitations

While PRISM demonstrates significant promise, we acknowledge several limitations that offer avenues for future research. Our current approach focuses specifically on identifying and pruning semantic redundancy based on feature correlation. It is not designed to detect other critical data issues, such as factual inaccuracies, ethical biases within the instruction data. Future work could explore extending our geometry-aware principles to address these other facets of data quality or adapting the method to new modalities beyond vision and language.

## References

Sanjeev Arora, Yuanzhi Li, Yingyu Liang, Tengyu Ma, and Andrej Risteski. 2016. **A latent variable model approach to PMI-based word embeddings**. In *Transactions of the Association for Computational Linguistics*, volume 4, pages 385–399.

Jinhe Bi, Yujun Wang, Haokun Chen, Xun Xiao, Artur Hecker, Volker Tresp, and Yunpu Ma. 2025a. **LLaVA steering: Visual instruction tuning with 500x fewer parameters through modality linear representation-steering**. In *Proceedings of the 63rd Annual Meeting of the Association for Computational Linguistics (Volume 1: Long Papers)*, pages 15230–15250, Vienna, Austria. Association for Computational Linguistics.

Jinhe Bi, Danqi Yan, Yifan Wang, Wenke Huang, Haokun Chen, Guancheng Wan, Mang Ye, Xun Xiao, Hinrich Schuetze, Volker Tresp, and 1 others. 2025b. **Cot-kinetics: A theoretical modeling assessing lrm reasoning process**. *arXiv preprint arXiv:2505.13408*.

Hao Chen, Yiming Zhang, Qi Zhang, Hantao Yang, Xiaomeng Hu, Xuetao Ma, Yifan Yanggong, and Junbo Zhao. 2023. **Maybe only 0.5% data is needed: A preliminary exploration of low training data instruction tuning**. *Preprint*, arXiv:2305.09246.

Haokun Chen, Hang Li, Yao Zhang, Jinhe Bi, Gengyuan Zhang, Yueqi Zhang, Philip Torr, Jindong Gu, Dennis Krompass, and Volker Tresp. 2025a. **Fedbip: Heterogeneous one-shot federated learning with personalized latent diffusion models**. In *Proceedings of the Computer Vision and Pattern Recognition Conference (CVPR)*, pages 30440–30450.

Haokun Chen, Yueqi Zhang, Yuan Bi, Yao Zhang, Tong Liu, Jinhe Bi, Jian Lan, Jindong Gu, Claudia Grosser, Denis Krompass, and 1 others. 2025b. **Does machine unlearning truly remove model knowledge? a framework for auditing unlearning in llms**. *arXiv preprint arXiv:2505.23270*.

Ruibo Chen, Yihan Wu, Lichang Chen, Guodong Liu, Qi He, Tianyi Xiong, Chenxi Liu, Junfeng Guo, and Heng Huang. 2024. **Your vision-language model itself is a strong filter: Towards high-quality instruction tuning with data selection**. *Preprint*, arXiv:2402.12501.

Zhe Chen, Weiyun Wang, Yue Cao, Yangzhou Liu, Zhangwei Gao, Erfei Cui, Jinguo Zhu, Shenglong Ye, Hao Tian, Zhaoyang Liu, Lixin Gu, Xuehui Wang, Qingyun Li, Yimin Ren, Zixuan Chen, Jiapeng Luo, Jiahao Wang, Tan Jiang, Bo Wang, and 23 others. 2025c. **Expanding performance boundaries of open-source multimodal models with model, data, and test-time scaling**. *Preprint*, arXiv:2412.05271.

Wenliang Dai, Junnan Li, Dongxu Li, Anthony Tiong, Junqi Zhao, Weisheng Wang, Boyang Li, Pascale Fung, and Steven Hoi. 2023. **InstructBLIP: Towards general-purpose vision-language models with instruction tuning**. In *Thirty-seventh Conference on Neural Information Processing Systems*.

Kawin Ethayarajh. 2019. **How contextual are contextualized word representations? Comparing the geometry of BERT, ELMo, and GPT-2 embeddings**. In *Proceedings of the 2019 Conference on Empirical Methods in Natural Language Processing and the 9th International Joint Conference on Natural Language Processing (EMNLP-IJCNLP)*, pages 55–65, Hong Kong, China. Association for Computational Linguistics.

Jiatao Gu, Zhipeng Chen, and Peter J. Liu. 2019. **Representation degeneration problem in training natural language generation models**. In *International Conference on Learning Representations (ICLR)*.

Danna Gurari, Qing Li, Abigale J. Stangl, Anhong Guo, Chi Lin, Kristen Grauman, Jiebo Luo, and Jeffrey P. Bigham. 2018. **Vizwiz grand challenge: Answering visual questions from blind people**. *Preprint*, arXiv:1802.08218.

Edward J. Hu, Yelong Shen, Phillip Wallis, Zeyuan Allen-Zhu, Yuanzhi Li, Shean Wang, Lu Wang, and Weizhu Chen. 2021. **LoRA: Low-rank adaptation of large language models**. *Preprint*, arXiv:2106.09685.

Kailin Jiang, Hongbo Jiang, Ning Jiang, Zhi Gao, Jinhe Bi, Yuchen Ren, Bin Li, Yuntao Du, Lei Liu, and Qing Li. 2025a. **Kore: Enhancing knowledge injection for large multimodal models via knowledge-oriented augmentations and constraints**. *Preprint*, arXiv:2510.19316.

Kailin Jiang, Ning Jiang, Yuntao Du, Yuchen Ren, Yuchen Li, Yifan Gao, Jinhe Bi, Yunpu Ma, Qingqing Liu, Xianhao Wang, Yifan Jia, Hongbo Jiang, Yaocong Hu, Bin Li, and Lei Liu. 2025b. **Mined: Probing and updating with multimodal time-sensitive knowledge for large multimodal models**. *Preprint*, arXiv:2510.19457.

Li Jing, Pascal Vincent, Yann LeCun, and Yuandong Tian. 2021. **Understanding dimensional collapse in contrastive self-supervised learning**. In *International Conference on Learning Representations (ICLR)*.

Jaewoo Lee, Boyang Li, and Sung Ju Hwang. 2024. **Concept-skill transferability-based data selection for large vision-language models.** *Preprint*, arXiv:2406.10995.

Meir Yossef Levi and Guy Gilboa. 2024. The double-ellipsoid geometry of clip. *arXiv preprint arXiv:2411.14517*.

Bo Li, Yuanhan Zhang, Dong Guo, Renrui Zhang, Feng Li, Hao Zhang, Kaichen Zhang, Peiyuan Zhang, Yanwei Li, Ziwei Liu, and Chunyuan Li. 2024. **Llava-onevision: Easy visual task transfer.** *Preprint*, arXiv:2408.03326.

Yifan Li, Yifan Du, Kun Zhou, Jinpeng Wang, Wayne Xin Zhao, and Ji-Rong Wen. 2023. **Evaluating object hallucination in large vision-language models.** *Preprint*, arXiv:2305.10355.

Haotian Liu, Chunyuan Li, Yuheng Li, and Yong Jae Lee. 2024a. **Improved baselines with visual instruction tuning.** *Preprint*, arXiv:2310.03744.

Haotian Liu, Chunyuan Li, Qingyang Wu, and Yong Jae Lee. 2024b. Visual instruction tuning. *Advances in neural information processing systems*, 36.

Yuan Liu, Haodong Duan, Yuanhan Zhang, Bo Li, Songyang Zhang, Wangbo Zhao, Yike Yuan, Jiaqi Wang, Conghui He, Ziwei Liu, Kai Chen, and Dahu Lin. 2024c. **Mmbench: Is your multi-modal model an all-around player?** *Preprint*, arXiv:2307.06281.

Zikang Liu, Kun Zhou, Wayne Xin Zhao, Dawei Gao, Yaliang Li, and Ji-Rong Wen. 2024d. **Less is more: High-value data selection for visual instruction tuning.** *Preprint*, arXiv:2403.09559.

Pan Lu, Swaroop Mishra, Tony Xia, Liang Qiu, Kai-Wei Chang, Song-Chun Zhu, Oyvind Tafjord, Peter Clark, and Ashwin Kalyan. 2022. Learn to explain: Multimodal reasoning via thought chains for science question answering. In *The 36th Conference on Neural Information Processing Systems (NeurIPS)*.

Rui Lu, Jinhe Bi, Yunpu Ma, Feng Xiao, Yuntao Du, and Yijun Tian. 2025. **Mv-debate: Multi-view agent debate with dynamic reflection gating for multimodal harmful content detection in social media.** *Preprint*, arXiv:2508.05557.

Mansheej Paul, Surya Ganguli, and Gintare Karolina Dziugaite. 2023. **Deep learning on a data diet: Finding important examples early in training.** *Preprint*, arXiv:2107.07075.

Alec Radford, Jong Wook Kim, Chris Hallacy, Aditya Ramesh, Gabriel Goh, Sandhini Agarwal, Girish Sastry, Amanda Askell, Pamela Mishkin, Jack Clark, Gretchen Krueger, and Ilya Sutskever. 2021. Learning transferable visual models from natural language supervision. In *Proceedings of the 38th International Conference on Machine Learning (ICML)*, volume 139, pages 8748–8763.

Xuankun Rong, Wenke Huang, Jian Liang, Jinhe Bi, Xun Xiao, Yiming Li, Bo Du, and Mang Ye. 2025. Backdoor cleaning without external guidance in mllm fine-tuning. *arXiv preprint arXiv:2505.16916*.

Yijun Tian, Shaoyu Chen, Zhichao Xu, Yawei Wang, Jinhe Bi, Peng Han, and Wei Wang. 2025. **Reinforcement mid-training.** *Preprint*, arXiv:2509.24375.

Shengbang Tong, Ellis Brown, Penghao Wu, Sanghyun Woo, Manoj Middepogu, Sai Charitha Akula, Jihan Yang, Shusheng Yang, Adithya Iyer, Xichen Pan, and 1 others. 2024. Cambrian-1: A fully open, vision-centric exploration of multimodal llms. *arXiv preprint arXiv:2406.16860*.

Weijie Wang, Bin Zhou, Mimi Li, and Xilin Chen. 2020. Understanding and improving vision and language representation learning. In *Proceedings of the 28th ACM International Conference on Multimedia*, pages 1737–1746.

Yujun Wang, Jinhe Bi, Yunpu Ma, and Soeren Pirk. 2025. **Ascd: Attention-steerable contrastive decoding for reducing hallucination in mllm.** *arXiv preprint arXiv:2506.14766*.

Lai Wei, Zihao Jiang, Weiran Huang, and Lichao Sun. 2023. **Instructiongpt-4: A 200-instruction paradigm for fine-tuning minigpt-4.** *Preprint*, arXiv:2308.12067.

Xindi Wu, Mengzhou Xia, Rulin Shao, Zhiwei Deng, Pang Wei Koh, and Olga Russakovsky. 2025. **Icons: Influence consensus for vision-language data selection.** *Preprint*, arXiv:2501.00654.

Mengzhou Xia, Sadhika Malladi, Suchin Gururangan, Sanjeev Arora, and Danqi Chen. 2024. **Less: Selecting influential data for targeted instruction tuning.** *Preprint*, arXiv:2402.04333.

Le Xue, Manli Shu, Anas Awadalla, Jun Wang, An Yan, Senthil Purushwalkam, Honglu Zhou, Viraj Prabhu, Yutong Dai, Michael S Ryoo, and 1 others. 2024. **xgen-mm (blip-3): A family of open large multimodal models.** *arXiv preprint arXiv:2408.08872*.

Shukang Yin, Chaoyou Fu, Sirui Zhao, Ke Li, Xing Sun, Tong Xu, and Enhong Chen. 2023. A survey on multimodal large language models. *arXiv preprint arXiv:2306.13549*.

Qifan Yu, Zhebei Shen, Zhongqi Yue, Yang Wu, Wenqiao Zhang, Yunfei Li, Juncheng Li, Siliang Tang, and Yueting Zhuang. 2024a. Mastering collaborative multi-modal data selection: A focus on informativeness, uniqueness, and representativeness. *arXiv preprint arXiv:2412.06293*.

Weihao Yu, Zhengyuan Yang, Linjie Li, Jianfeng Wang, Kevin Lin, Zicheng Liu, Xinchao Wang, and Lijuan Wang. 2024b. **Mm-vet: Evaluating large multimodal models for integrated capabilities.** *Preprint*, arXiv:2308.02490.

Xiang Yue, Yuansheng Ni, Kai Zhang, Tianyu Zheng, Ruoqi Liu, Ge Zhang, Samuel Stevens, Dongfu Jiang, Weiming Ren, Yuxuan Sun, Cong Wei, Botao Yu, Ruibin Yuan, Renliang Sun, Ming Yin, Boyuan Zheng, Zhenzhu Yang, Yibo Liu, Wenhao Huang, and 3 others. 2024. **Mmmu: A massive multi-discipline multimodal understanding and reasoning benchmark for expert agi.** *Preprint*, arXiv:2311.16502.

Gengyuan Zhang, Jinhe Bi, Jindong Gu, Yanyu Chen, and Volker Tresp. 2023. Spot! revisiting video-language models for event understanding. *arXiv preprint arXiv:2311.12919*.

Yan Zhang, Ruidan He, Zuozhu Liu, Kwan Hui Lim, and Lidong Bing. 2020. **An unsupervised sentence embedding method by mutual information maximization.** In *Proceedings of the 2020 Conference on Empirical Methods in Natural Language Processing (EMNLP)*, pages 1601–1610, Online. Association for Computational Linguistics.

Yi-Kai Zhang, Shiyin Lu, Yang Li, Yanqing Ma, Qing-Guo Chen, Zhao Xu, Weihua Luo, Kaifu Zhang, De-Chuan Zhan, and Han-Jia Ye. 2024. **Wings: Learning multimodal llms without text-only forgetting.** *Preprint*, arXiv:2406.03496.

Chunting Zhou, Pengfei Liu, Puxin Xu, Srinivasan Iyer, Jiao Sun, Yuning Mao, Xuezhe Ma, Avia Efrat, Ping Yu, Lili Yu, and 1 others. 2024. Lima: Less is more for alignment. *Advances in Neural Information Processing Systems*, 36.

Deyao Zhu, Jun Chen, Xiaoqian Shen, Xiang Li, and Mohamed Elhoseiny. 2023. **Minigpt-4: Enhancing vision-language understanding with advanced large language models.** *Preprint*, arXiv:2304.10592.

## A Related Work

**Visual Instruction Tuning:** Visual instruction tuning is essential for aligning MLLMs with both practical applications and academic benchmarks. Early methods relied on synthetic visual instructions, which performed well in conversations but struggled on rigorous benchmarks. A hybrid approach later emerged, integrating synthetic data with academic datasets to improve training diversity. This advancement has enhanced models like LLaVA (Liu et al., 2024b), InstructBLIP (Dai et al., 2023), and Cambrian (Tong et al., 2024), enabling better visual-linguistic understanding. Beyond task performance, visual instruction tuning improves model alignment with user expectations, ensuring both practical utility and strong academic performance.

**Visual Instruction Selection:** Despite the strong performance of MLLMs, the rapid growth of visual instruction datasets has introduced significant redundancy, similar to challenges in LLMs (Zhou et al., 2024; Chen et al., 2023; Xia et al., 2024; Tian et al., 2025; Lu et al., 2025; Bi et al., 2025b). State-of-the-art models like BLIP3 (Xue et al., 2024), InternVL2.5 (Chen et al., 2025c), and LLaVA-OneVision (Li et al., 2024) rely on billions of instructions to enhance understanding, but their massive scale leads to substantial computational costs, often requiring hundreds to thousands of GPU hours.

To address this, various data selection strategies aim to reduce redundancy while preserving performance. TIVE (Liu et al., 2024d) selects valuable data based on gradient similarity but requires additional training on downstream tasks. SELF-FILTER (Chen et al., 2024) uses an auxiliary evaluation model to prioritize high-value samples. COINCIDE (Lee et al., 2024) clusters data by conceptual and skill-based representations, while InstructionGPT-4 (Wei et al., 2023) filters 200 instructions for MiniGPT-4 (Zhu et al., 2023), though it lacks scalability. ICONS (Wu et al., 2025) extends LESS (Xia et al., 2024) by incorporating specialist influence estimation for instruction tuning. DataTailor (Yu et al., 2024a) selects data based on informativeness, uniqueness, and representativeness to retain the most relevant samples.

## B Dataset and Selection Details

This section provides a detailed breakdown of our PRISM-Instruct-250K dataset and the underlying

data distributions that informed its creation. The dataset is the result of applying the PRISM selection methodology to the LLaVA-665K data pool, which aggregates samples from diverse sources. Our goal is to create a compact, high-utility subset by retaining the most informative, low-redundancy samples.

### B.1 Redundancy Score Distribution

At the core of our selection process is the *Redundancy Score*  $\mathcal{R}(d_i)$ , which quantifies the degree to which a sample is semantically similar to the rest of the corpus. Figure 7 visualizes the distribution of these scores (lower is better) for each source dataset within the LLaVA-665K pool.

The distributions reveal the varying levels of internal diversity within each source. For instance, datasets like LLaVA and VG exhibit a wider distribution with a significant number of low-score (high-value) samples. In contrast, other datasets may have a higher density of redundant, high-score samples. PRISM applies a single, global threshold to this combined pool, ensuring that only the top 30% of samples—those with the lowest redundancy scores, regardless of their origin—are selected. This principled approach prevents any single, potentially redundant dataset from dominating the final selection and instead curates a subset based on universal informational value.

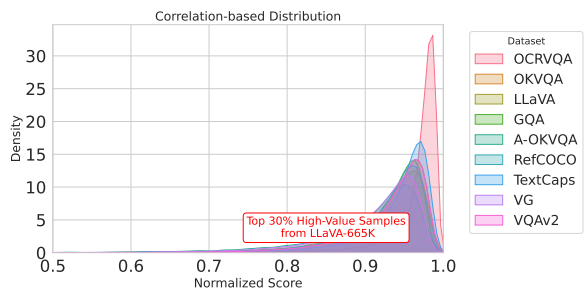


Figure 7: **Distribution of PRISM’s Redundancy Scores across source datasets.** The vertical line indicates the global selection threshold used to prune the 70% most redundant samples (i.e., those with the highest correlation scores). Datasets with a higher density of low-correlation samples contribute more instances to the final PRISM-Instruct-250K set, ensuring a merit-based composition.

### B.2 Final Dataset Composition

The application of our selection strategy results in the PRISM-Instruct-250K dataset. Table 4 details the final number of samples drawn from each



**Top-Ranked Sample**

[Question] What region of the world is this located?

[Answer] Asia

[Reasoning] Requires fine-grained OCR and cultural reasoning.



**Bottom-Ranked Sample**

[Question] What type of weather is this?

[Answer] Sunny

[Reasoning] Trivial perception; high semantic redundancy.

Figure 8: **Representative examples selected by PRISM from LLaVA-665K.** Top-ranked samples correspond to more challenging and informative interactions that exhibit unique semantic structures, whereas bottom-ranked samples tend to be trivial, binary, or semantically redundant.

source. The composition reflects the data-driven nature of our method: sources rich in unique, low-correlation samples are more heavily represented. The result is a balanced and diverse instruction-tuning dataset that has been algorithmically optimized for both performance and efficiency.

Data Source	Number of Samples
LLaVA	53,591
VQAv2	27,567
OKVQA	2,997
A-OKVQA	22,032
RefCOCO	16,933
VG	28,777
GQA	24,023
OCRVQA	26,638
TextCaps	7,311
Text-Only	40,688
<b>Total</b>	<b>250,557</b>

Table 4: Final sample distribution of the PRISM-Instruct-250K dataset after applying our selection methodology to the LLaVA-665K pool.

### B.3 Qualitative Analysis of PRISM Selection

To provide a more intuitive understanding of the Intrinsic Selection paradigm, we conduct a qualitative analysis of samples ranked by PRISM. Figure 8 illustrates representative examples from the top-ranked (selected) and bottom-ranked (pruned) tiers of the LLaVA-665K dataset.

#### B.3.1 High-Value: Challenging and Informative

The top-ranked samples prioritized by PRISM typically involve **fine-grained perception** and **complex contextual reasoning**. For instance, in the "Asia street" example (Figure 8, Left), the model must identify localized visual cues such as the road marking Tomare, the specific structure of utility poles, and architectural styles to correctly determine the geographical region. From a training perspective, these informative interactions provide a stronger learning signal, often corresponding to higher initial loss values, which is critical for mastering expert-level reasoning.

#### B.3.2 Low-Value: Trivial and Redundant

Conversely, bottom-ranked samples are frequently characterized by **trivial perception** or **high semantic redundancy**. In the "Sunny weather" example (Figure 8, Right), the task involves identifying a generic weather condition in a common park setting. Such visual scenes—comprising grass, trees, and sunlight—are over-represented in the corpus, leading to a high correlation with the Global Semantic Drift.

Because these samples offer saturated information and redundant gradients, training on them yields diminishing returns and may even exacerbate "knowledge forgetting". By pruning these trivial samples, PRISM ensures a more efficient

use of the computational budget without sacrificing model performance.

## C Model Architecture Details and Generalization Setup

To rigorously evaluate the generalization capabilities of PRISM, we extend our analysis across a diverse set of Multimodal Large Language Models (MLLMs). The objective is to verify whether the visual anisotropy diagnosis and the subsequent performance gains from PRISM remain consistent across different model scales, language model families, and vision encoder architectures. This broad evaluation ensures that the intrinsic semantic properties identified by PRISM are not artifacts of a specific model configuration but represent fundamental characteristics of multimodal data representations.

As summarized in Table 5, our evaluation framework encompasses the following dimensions:

- **Language Model Families and Scales:** Beyond the Vicuna and Phi-2 families discussed in the main text, we include the Qwen2.5 series (7B Base and Instruct) and Llama-3 (8B) to represent state-of-the-art open-source LLM backbones.
- **Vision Encoders:** We evaluate models utilizing various vision foundation backbones, specifically CLIP ViT-L/14 (336px) and SigLIP-SO400M, to ensure PRISM’s robustness to different cross-modal alignment strategies.
- **Generalization Analysis:** For each configuration, we conduct both a systematic anisotropy diagnosis (as detailed in Section 3.2) and an end-to-end evaluation of the performance improvements yielded by PRISM-selected data.

Model Family	Vision Encoder	Language Model Backbone
LLaVA-Vicuna-7B	CLIP ViT-L/14 (336px)	Vicuna v1.5 7B
LLaVA-Phi2-3B	SigLIP-SO400M	Phi-2 2.7B
LLaVA-Vicuna-13B	CLIP ViT-L/14 (336px)	Vicuna v1.5 13B
LLaVA-Qwen-7B	SigLIP-SO400M	Qwen2.5-7B (Base/Instruct)
LLaVA-Llama-8B	CLIP ViT-L/14 (336px)	Llama-3-8B

**Table 5: Comprehensive architectural configurations for generalization testing.** The evaluation spans multiple LLM families, varying parameter scales, and diverse vision encoders to validate the universal applicability of PRISM.

## D Impact of Textual Representation and Joint Multimodal Selection

To address potential concerns regarding the role of textual prompts in data redundancy, this section provides: (1) a comparative analysis of visual vs. textual anisotropy, (2) the motivation for our visual-centric approach, and (3) additional experimental results explicitly incorporating textual features during selection.

### D.1 Contrastive Anisotropy: Visual vs. Textual Modalities

Our diagnosis of representation anisotropy reveals a significant disparity between modalities. As illustrated in Figure 2, while visual features across all instruction datasets exhibit a non-zero mean vector  $\mu$  with substantial magnitude, text features produced by the same MLLM are comparatively well-centered around the origin. Furthermore, the singular value spectrum of the textual embedding space is considerably flatter than that of the visual space.

Because these two modalities exhibit fundamentally different geometric behaviors, applying a single global re-centering operation to concatenated multimodal features would be suboptimal. A joint mean vector would be dominated by the severe visual drift, potentially over-correcting or distorting the near-isotropic textual geometry, thereby degrading the quality of similarity estimates. Consequently, PRISM focuses its geometric correction on the visual stream, where anisotropy is the primary obstacle to redundancy detection.

### D.2 Primacy of Visual Redundancy in Instruction Tuning

In the context of visual instruction tuning, the image typically serves as the primary carrier of new scene-level semantics. In datasets such as LLaVA-665K, text prompts often function as task-specific templates (e.g., questions or instructions) conditioned on the visual content. Therefore, redundancy in these datasets is largely governed by the visual channel: models frequently encounter near-identical visual semantics under slight variations of textual phrasing. By targeting visual anisotropy, PRISM effectively prunes redundant visual scenes that provide diminishing returns during the fine-tuning process.

### D.3 Additional Experiments with Multimodal Features

To empirically verify this design choice, we conducted additional experiments on LLaVA-1.5-7B using features that explicitly incorporate both visual and textual information. We constructed multimodal representations by aggregating image tokens and text prompt tokens before applying the PRISM selection pipeline.

As shown in Table 7, including textual prompts in the selection signal does not yield performance gains over our visual-only approach. In fact, the multimodal-feature selection (97.8% relative performance) underperforms the visual-only PRISM (101.7%). We hypothesize this is because text prompts introduce additional variance related to syntactic style and template length that is uncorrelated with the underlying semantic redundancy of the task. These results reinforce that visual anisotropy is the dominant factor to address for training-free intrinsic selection.

## E Limitations of Existing Methods and Our Geometric Motivation

This section provides a detailed analysis of the structural limitations inherent in existing visual instruction selection paradigms and introduces the theoretical motivation for our work. We first outline the three primary failure modes of prior methods and then present our diagnosis that these issues stem from a single, unaddressed geometric flaw in MLLM feature representations.

### E.1 A Critical Review of Existing Selection Paradigms

Despite their diverse approaches, current selection methods consistently exhibit three critical drawbacks that limit their practical utility, often violating the core principles of effective data selection we established in Section 2.

**1. Performance Degradation.** A primary goal of data selection is to curate a smaller, more potent dataset that ideally improves model performance. However, as shown in our main results (Table 1), many existing methods paradoxically lead to models that underperform a full fine-tuning baseline. This outcome directly contradicts our *Principle 1 (Performance Fidelity)*, suggesting that their heuristics for identifying "valuable" data are often misaligned with the true learning objectives.

**2. Prohibitive Computational Cost.** The second

major failure mode is excessive computational overhead, particularly in Training-Based methods. For instance, techniques like TIVE (Liu et al., 2024d) require a costly "warm-up" phase, often involving LoRA-based (Hu et al., 2021; Bi et al., 2025a) fine-tuning, simply to generate the gradient signals needed for selection. As we show in our runtime analysis (Table 13), the time spent on selection alone can exceed the time saved during the subsequent tuning, violating *Principle 2 (Net Efficiency Gain)* and rendering the approach impractical at scale.

**3. Proxy Model Bias.** To avoid the high costs of gradient computation, some methods delegate scoring to an external proxy model (e.g., GPT-4 or a reward model). While faster, this introduces a significant bias, as the proxy's scoring function may not align with the target MLLM's specific learning needs. This approach yields a generic, one-size-fits-all dataset, failing to provide an optimal, tailored subset for the specific MLLM being trained.

### E.2 The Unifying Cause: A Deep Dive into Representation Anisotropy

We argue that these seemingly disparate issues are symptoms of a single, deeper problem: a failure to account for the pathological geometry of MLLM feature spaces. In practice, high-dimensional embeddings learned by deep networks are rarely isotropic (uniformly distributed); instead, they are highly **anisotropic**, exhibiting a strong directional bias that corrupts the very notion of semantic distance and plagues models across modalities (Ethayarajh, 2019; Gu et al., 2019; Jing et al., 2021; Jiang et al., 2025b,a; Chen et al., 2025b,a; Zhang et al., 2023; Rong et al., 2025; Wang et al., 2025).

**The Geometry of Anisotropy.** An embedding space is said to be **isotropic** if its features are, on average, uniformly distributed in all directions from the origin. For a zero-mean feature set  $\mathcal{X} = \{\mathbf{x}_i\}$ , this property is formally defined by a covariance matrix proportional to the identity matrix,  $\mathbb{E}[\mathbf{x}\mathbf{x}^\top] \propto \mathbf{I}$ . Such a space leverages its full dimensionality to represent concepts. In stark contrast, an **anisotropic** space is characterized by a non-uniform, biased distribution.

**Low Effective Rank and Representation Degeneration.** A complementary perspective comes from singular value decomposition (SVD). In an anisotropic space, the singular value spectrum of the centered feature matrix exhibits a sharp, steep

Model	SQA	SQA-I	VizWiz	POPE-P	POPE-R	POPE-A	MM-Vet	MMBench	MME	MMMU	Rel. (%)
LLaVA-Phi2-3B	75.3	72.7	41.2	87.3	88.6	86.1	35.6	68.7	1765.7	37.7	100%
PRISM-3B	<b>76.3</b>	<b>72.8</b>	40.9	<b>87.5</b>	<b>88.8</b>	<b>86.5</b>	34.1	<b>68.9</b>	<b>1790.5</b>	37.6	<b>100.1%</b>
LLaVA-Vicuna-7B	69.4	66.8	50.0	86.1	87.3	84.2	31.1	64.3	1822.6	35.4	100%
PRISM-7B	<b>71.3</b>	<b>69.1</b>	<b>50.1</b>	<b>87.7</b>	<b>88.7</b>	<b>85.5</b>	<b>32.0</b>	<b>65.2</b>	<b>1800.0</b>	34.7	<b>101.7%</b>
LLaVA-Vicuna-13B	74.4	71.6	53.6	87.4	88.0	85.6	36.1	67.7	1826.7	35.1	100%
PRISM-13B	<b>74.5</b>	<b>71.8</b>	53.1	<b>87.7</b>	<b>88.4</b>	<b>85.7</b>	<b>36.4</b>	65.8	<b>1846.0</b>	<b>35.7</b>	<b>100.4%</b>
LLaVA-Qwen-7B (Base)	79.1	76.7	55.3	87.3	89.1	86.4	33.1	70.1	1923.1	46.0	100%
PRISM-Qwen-7B (Base)	<b>81.2</b>	<b>78.9</b>	55.1	<b>88.6</b>	<b>90.3</b>	<b>87.5</b>	<b>33.7</b>	<b>71.5</b>	<b>1895.8</b>	45.2	<b>101.0%</b>
LLaVA-Qwen-7B (Instruct)	80.2	77.8	54.7	87.9	89.7	86.9	33.8	71.0	1935.4	46.8	100%
PRISM-Qwen-7B (Instruct)	<b>82.3</b>	<b>80.1</b>	54.2	<b>89.1</b>	<b>90.8</b>	<b>88.1</b>	<b>34.2</b>	<b>72.4</b>	<b>1908.6</b>	46.1	<b>100.9%</b>
LLaVA-Llama-8B	77.6	75.2	53.7	86.3	87.6	84.0	31.8	68.5	1889.7	40.3	100%
PRISM-Llama-8B	<b>79.4</b>	<b>77.3</b>	53.4	<b>87.8</b>	<b>89.1</b>	<b>85.6</b>	31.5	<b>69.9</b>	<b>1862.5</b>	39.7	<b>100.8%</b>

Table 6: **Cross-Model Generalization and Scalability of PRISM.** PRISM’s selection mechanism generalizes robustly across diverse MLLM architectures by correcting representation anisotropy, as shown across five LLaVA-style model–encoder combinations. By identifying semantically dense samples for each architecture, PRISM consistently improves performance over full finetuning for both small and large language models—including Vicuna, Phi-2, Qwen2.5, and Llama-3—as well as distinct vision encoders such as CLIP and SigLIP. Together with Fig. 5, these results confirm that PRISM’s gains are not tied to a particular LLaVA configuration but transfer across diverse multimodal model families.

Method	SQA	SQA-I	VizWiz	POPE-P	POPE-R	POPE-A	MM-Vet	MMBench	MME-P	MME-C	MMMU	Rel. (%)
Full-Finetune	69.4	66.8	50.0	86.1	87.3	84.2	31.1	64.3	1510.7	311.9	35.4	100%
Multimodal PRISM	68.2	65.1	48.9	85.3	86.0	83.1	30.2	63.0	1455.0	305.0	34.1	97.8%
✓ Visual-only PRISM	<b>71.3</b>	<b>69.1</b>	<b>50.1</b>	<b>87.7</b>	<b>88.7</b>	<b>85.5</b>	<b>32.0</b>	<b>65.2</b>	1470.0	<b>330.0</b>	34.7	<b>101.7%</b>

Table 7: **Comparison of selection using visual-only features versus joint multimodal features.** The visual-centric approach (PRISM) demonstrates higher stability as text prompts often introduce non-semantic noise.

decay. As illustrated in Figure 2, a few dominant singular values capture most of the data’s variance, while the rest are negligible. This indicates a **low effective rank** (Arora et al., 2016), meaning the representation fails to utilize the full capacity of its embedding dimensions. This phenomenon, often called **representation degeneration**, is prevalent in modern architectures, including those trained with contrastive objectives like CLIP (Radford et al., 2021; Wang et al., 2020).

**Implications for Data Selection.** This unaddressed geometric flaw directly explains the failures of prior art. Because simple and efficient geometric metrics (e.g., cosine similarity, farthest-point sampling) are rendered useless by anisotropy, existing methods are forced to adopt computationally expensive proxies to approximate “true” semantic value. Training-Based methods pay a heavy price in computation to derive signals from the model’s dynamics, while Proxy-Based methods introduce potential biases from an external scorer. Both are, in effect, paying a high computational “tax” for failing to first correct the geometry of the space itself. Our work is motivated by the insight that by directly diagnosing and correcting this anisotropy, we can unlock a far more efficient and

principled path to data selection that operates on the intrinsic, geometrically-sound structure of the data.

## F Theoretical Foundation: Anisotropy as a Source of Computational Overhead

This section provides a rigorous theoretical analysis of why existing data selection methods for MLLMs are inherently inefficient. We formalize the concept of representation anisotropy and prove that it renders simple geometric metrics useless for measuring semantic diversity. As a direct consequence, we show that any algorithm operating in such a flawed space must resort to computationally expensive proxies, thus explaining the high costs of prior art and motivating our geometry-aware approach.

### F.1 The Geometric Pathology of Anisotropy

We begin by formalizing the geometric properties of the feature space. Let  $\phi : \mathcal{D} \rightarrow \mathbb{R}^d$  be the MLLM’s embedding function. The observed anisotropy in the visual feature space implies a non-zero mean vector  $\mu = \mathbb{E}[\phi(d)]$  with a large magnitude. Consequently, any feature vector  $\mathbf{x}_i = \phi(d_i)$  can be decomposed into a shared, dominant global

component and a sample-specific semantic residual:

$$\mathbf{x}_i = \boldsymbol{\mu} + \boldsymbol{\delta}_i \quad (8)$$

where  $\boldsymbol{\delta}_i$  encodes the unique semantics of sample  $d_i$ . The defining characteristic of a highly anisotropic space is that this shared component dominates the representation, i.e.,  $\|\boldsymbol{\mu}\|_2 \gg \mathbb{E}[\|\boldsymbol{\delta}_i\|_2]$ . This property has a catastrophic consequence for standard geometric metrics, which we formalize in the following theorem.

**Theorem 3** (Corruption of Geometric Proximity). *In an anisotropic representation space where  $\|\boldsymbol{\mu}\|_2 \gg \mathbb{E}[\|\boldsymbol{\delta}_i\|_2]$ , the cosine similarity between any two randomly sampled vectors  $\mathbf{x}_i$  and  $\mathbf{x}_j$  is dominated by the global drift vector  $\boldsymbol{\mu}$ , masking their true semantic dissimilarity, which is encoded in the residuals  $\boldsymbol{\delta}_i, \boldsymbol{\delta}_j$ .*

*Proof.* The cosine similarity is given by:

$$\cos(\mathbf{x}_i, \mathbf{x}_j) = \frac{(\boldsymbol{\mu} + \boldsymbol{\delta}_i)^\top (\boldsymbol{\mu} + \boldsymbol{\delta}_j)}{\|\boldsymbol{\mu} + \boldsymbol{\delta}_i\|_2 \|\boldsymbol{\mu} + \boldsymbol{\delta}_j\|_2} \quad (9)$$

The numerator expands to  $\|\boldsymbol{\mu}\|_2^2 + \boldsymbol{\mu}^\top (\boldsymbol{\delta}_i + \boldsymbol{\delta}_j) + \boldsymbol{\delta}_i^\top \boldsymbol{\delta}_j$ . Since  $\|\boldsymbol{\mu}\|_2$  is the dominant term, the denominator can be approximated using a first-order Taylor expansion as  $\|\boldsymbol{\mu} + \boldsymbol{\delta}_i\|_2 \approx \|\boldsymbol{\mu}\|_2 + \frac{\boldsymbol{\mu}^\top \boldsymbol{\delta}_i}{\|\boldsymbol{\mu}\|_2}$ . Substituting these approximations and retaining only the leading-order terms yields:

$$\begin{aligned} \cos(\mathbf{x}_i, \mathbf{x}_j) &\approx \frac{\|\boldsymbol{\mu}\|_2^2}{\left(\|\boldsymbol{\mu}\|_2 + \frac{\boldsymbol{\mu}^\top \boldsymbol{\delta}_i}{\|\boldsymbol{\mu}\|_2}\right) \left(\|\boldsymbol{\mu}\|_2 + \frac{\boldsymbol{\mu}^\top \boldsymbol{\delta}_j}{\|\boldsymbol{\mu}\|_2}\right)} \\ &\approx 1 - \frac{1}{2} \left\| \frac{\boldsymbol{\delta}'_i}{\|\boldsymbol{\mu}\|_2} - \frac{\boldsymbol{\delta}'_j}{\|\boldsymbol{\mu}\|_2} \right\|_2^2 \approx 1 \end{aligned} \quad (10)$$

where  $\boldsymbol{\delta}'$  is the component of  $\boldsymbol{\delta}$  orthogonal to  $\boldsymbol{\mu}$ . The true semantic similarity, proportional to  $\boldsymbol{\delta}_i^\top \boldsymbol{\delta}_j$ , is relegated to lower-order terms that are numerically insignificant, rendering the metric incapable of distinguishing unique samples.  $\square$

## F.2 The Inevitable Complexity of Anisotropic Selection

The failure of simple geometric proxies, as established in Theorem 3, creates a fundamental dilemma. To select a diverse subset, an algorithm cannot rely on efficient distance calculations in the raw feature space. It is therefore forced to adopt more complex, computationally intensive strategies to approximate the true, latent semantic structure of the data.

**Theorem 4** (The Computational Cost of Anisotropic Selection). *To recover semantic diversity in an anisotropic space, a selection algorithm must resort to computationally expensive proxies that scale super-linearly with dataset size  $N$ . Common strategies include:*

1. **Implicit Structure Recovery:** *Employing clustering algorithms to recover latent semantic groups in the distorted space, incurring a computational cost of at least  $\mathcal{O}(I \cdot N \cdot K \cdot d)$ , where  $I$  is the number of iterations and  $K$  is the number of clusters.*

2. **Bypassing Geometry via Training Dynamics:** *Using model gradients or training loss as a proxy for data value, incurring a cost of at least  $\mathcal{O}(N \cdot C_{\text{pass}})$ , where  $C_{\text{pass}}$  is the cost of a full forward and backward model pass.*

*Proof.* (1) Because geometric proximity in an anisotropic space does not correlate with semantic similarity, algorithms must explicitly attempt to discover the latent semantic clusters. A standard approach like K-Means requires an iterative process of assignment and re-centering, the cost of which scales with the number of iterations, data points, clusters, and the feature dimension.

(2) Alternatively, methods like GraNd (Paul et al., 2023) and TIVE (Liu et al., 2024d) bypass the flawed geometry entirely by using signals from the model’s training dynamics. This requires at least one forward and/or backward pass per sample to compute gradients or loss values. The cost of a single pass,  $C_{\text{pass}}$ , scales with the number of model parameters  $P$ , which is typically orders of magnitude larger than the feature dimension  $d$ .

Both strategies are computationally prohibitive compared to the simple, near-linear time geometric methods (e.g., farthest-point sampling) that would suffice in an isotropic space. This analysis reveals that the high computational cost of existing methods is not an incidental flaw but an **inevitable consequence** of their failure to address the underlying geometric pathology of the feature space.  $\square$

## G Cross-Architecture Diagnosis of Representation Anisotropy

To further validate that representation anisotropy is a universal characteristic of Multimodal Large Language Models (MLLMs), we expand our diagnostic analysis across five distinct model-encoder combinations. This section provides detailed statistical

distributions of per-dimension means to characterize the geometric shift in the feature space.

### G.1 Metric Definitions

We utilize the following statistics to quantify the distribution of per-dimension means across different datasets:

- **Min / Max:** The extreme values of the per-dimension mean vectors.
- **Mean( $|x|$ ):** The arithmetic mean of the absolute per-dimension means, serving as a primary indicator of the magnitude of the global shift from the origin.
- **Percentiles (P25, P75, P99):** Values representing the spread and skewness of the mean distribution across dimensions.

### G.2 Per-dimension Mean Statistics across Configurations

Tables 8 through 11 present the statistics for diverse language backbones and vision encoders. Across all configurations, a consistent pattern emerges: textual features remain well-centered around zero ( $\text{Mean}(|x|) \approx 0.11\text{--}0.13$ ), whereas all visual instruction datasets exhibit substantial non-zero shifts ( $\text{Mean}(|x|) \approx 0.36\text{--}0.66$ ).

Table 8: Statistics for Vicuna v1.5 7B + CLIP ViT-L/14 336px.

Dataset	Min	P25	P75	P99	Max	Mean( $ x $ )
Text	-2.8851	-0.1033	0.0064	0.1105	0.3956	0.1310
A-OKVQA	-4.0186	-0.3351	0.0052	0.3329	1.2545	0.4045
GQA	-4.0984	-0.3448	0.0057	0.3404	1.2815	0.4141
LLaVA	-4.0885	-0.3427	0.0046	0.3394	1.2819	0.4126
OCRVQA	-5.6103	-0.5129	0.0023	0.5187	1.8318	0.6127
VG	-4.1034	-0.3449	0.0062	0.3413	1.2827	0.4147

Table 9: Statistics for Phi-2 2.7B + SigLIP-SO400M-Patch14-384.

Dataset	Min	P25	P75	P99	Max	Mean( $ x $ )
Text	-2.9124	-0.1047	0.0072	0.1119	0.4012	0.1328
A-OKVQA	-4.3215	-0.3587	0.0048	0.3612	1.3421	0.4384
GQA	-4.4102	-0.3701	0.0053	0.3689	1.3745	0.4501
LLaVA	-4.4018	-0.3675	0.0042	0.3668	1.3751	0.4483
OCRVQA	-6.0321	-0.5514	0.0019	0.5589	1.9647	0.6589
VG	-4.4147	-0.3704	0.0058	0.3695	1.3754	0.4505

### G.3 Architectural Generality and Observations

The results demonstrate that representation anisotropy is a robust and persistent phenomenon

Table 10: Statistics for Qwen2.5 7B Base + CLIP ViT-L/14 336px.

Dataset	Min	P25	P75	P99	Max	Mean( $ x $ )
Text	-2.6734	-0.0891	0.0058	0.0945	0.3512	0.1089
A-OKVQA	-3.7845	-0.3012	0.0047	0.3089	1.1523	0.3698
GQA	-3.8621	-0.3101	0.0052	0.3154	1.1789	0.3789
LLaVA	-3.8534	-0.3079	0.0041	0.3147	1.1793	0.3776
OCRVQA	-5.1987	-0.4687	0.0021	0.4823	1.6845	0.5634
VG	-3.8665	-0.3104	0.0056	0.3162	1.1795	0.3793

Table 11: Statistics for Llama-3-8B + CLIP ViT-L/14 336px.

Dataset	Min	P25	P75	P99	Max	Mean( $ x $ )
Text	-2.6512	-0.0876	0.0055	0.0929	0.3445	0.1067
A-OKVQA	-3.7621	-0.2989	0.0046	0.3067	1.1434	0.3667
GQA	-3.8389	-0.3078	0.0051	0.3132	1.1701	0.3756
LLaVA	-3.8301	-0.3056	0.0040	0.3125	1.1705	0.3743
OCRVQA	-5.1623	-0.4634	0.0020	0.4789	1.6712	0.5589
VG	-3.8432	-0.3081	0.0055	0.3140	1.1707	0.3760

across different language backbones (Vicuna, Phi-2, Qwen, Llama) and vision encoders (CLIP, SigLIP). While more advanced language models slightly reduce the absolute magnitude of visual anisotropy (e.g., Llama-3 and Qwen show approximately 10% lower Mean( $|x|$ ) than Vicuna), the visual-textual gap remains pronounced in all cases. This evidence confirms that the geometric origins of Global Semantic Drift are general to the MLLM architecture and are not specific to the LLaVA framework.

## H Benchmark Details

We provide detailed descriptions of the seven multimodal benchmarks used in our main evaluation.

**MMBench** (Liu et al., 2024c) is a multi-faceted benchmark that evaluates the all-around capabilities of MLLMs. It assesses both perception and reasoning through single-choice questions organized hierarchically across a wide range of domains.

**ScienceQA** (Lu et al., 2022) evaluates scientific question answering. It features multimodal questions from various science domains that require models to jointly reason over visual and textual contexts, often involving diagrams, charts, and complex text.

**MME** (Yin et al., 2023) is a comprehensive benchmark designed to assess multimodal reasoning and perception skills. It comprises 14 sub-tasks that cover a broad spectrum of capabilities, from object existence and position to text translation and code reasoning.

**POPE** (Li et al., 2023) is an evaluation framework

specifically designed to measure object hallucination in MLLMs. It uses a polling-based (Yes/No) question-answering approach to probe whether a model falsely perceives objects that are not present in an image.

**VizWiz** (Gurari et al., 2018) tests a model’s ability to answer visual questions taken “in-the-wild” by visually impaired users. It serves as a challenging test for zero-shot generalization, as the questions and images are often unconventional and noisy.

**MM-Vet** (Yu et al., 2024b) is an evaluation benchmark designed to measure the emergent, instruction-following capabilities of MLLMs in a multimodal context. It assesses a model’s ability to handle complex prompts that integrate perception, reasoning, and world knowledge.

**MMMU** (Yue et al., 2024) is a massive, multi-discipline benchmark that assesses expert-level MLLM capabilities. It requires the integration of perception, knowledge, and reasoning across a wide array of college-level subjects, from science and engineering to arts and humanities.

## I Sensitivity Analysis of the Selection Ratio

In this section, we provide a detailed sensitivity analysis of the selection ratio  $\tau$ , which governs the proportion of data retained for instruction tuning. Unlike static hyperparameters,  $\tau$  serves as a flexible selection budget that practitioners can adjust based on specific computational constraints. Table 12 presents the performance trade-offs across various sampling ratios. Our analysis reveals that PRISM is robust across diverse selection budgets:

- **Monotonic Visual Scaling:** Multimodal performance scales consistently with the data budget, with the 30% ratio (PRISM-Instruct-250K) effectively surpassing the full-dataset baseline.
- **Language Capability Preservation:** Textual performance remains remarkably high even at extreme pruning levels (e.g., 5%), suggesting that PRISM’s redundancy identification excels at isolating a high-quality “data core” that minimizes catastrophic forgetting.

## J Selection Metric Rationale: Correlation vs. Second-Order Distance

The design of PRISM prioritizes a training-free, computationally efficient pipeline. While second-

Sampling Ratio ( $\tau$ )	Visual Performance	Textual Performance
5%	92.3	104.4
10%	95.1	102.9
20%	97.1	102.1
✓ 30% (PRISM Default)	101.7	101.9
Full Fine-tuning (Baseline)	100.0	100.0

Table 12: **Performance robustness across varied selection ratios  $\tau$ .** Visual performance denotes the relative average score across multimodal benchmarks, while textual performance reflects foundational language understanding scores relative to the baseline.

order measures like Mahalanobis distance are theoretically relevant to anisotropy, they introduce significant bottlenecks in large-scale multimodal settings. We justify the use of implicit re-centering via Pearson correlation based on the following factors:

## J.1 Algorithmic Efficiency and Scalability

The estimation of Mahalanobis distance requires the computation and inversion of a covariance matrix  $\Sigma \in \mathbb{R}^{d \times d}$ . For modern MLLMs with high-dimensional feature spaces, this incurs an  $\mathcal{O}(Nd^2)$  cost for estimation and  $\mathcal{O}(d^3)$  for inversion. In contrast, PRISM’s correlation-based scoring operates with near-linear complexity relative to the feature dimension, enabling the processing of the LLaVA-665K dataset in just 1.5 GPU hours.

## J.2 Numerical Stability in Anisotropic Spaces

Our singular value analysis demonstrates that pre-trained visual features occupy a low effective rank, where variance is concentrated in a few dominant dimensions. This geometric degeneration often results in ill-conditioned covariance matrices. Relying on matrix inversion in such spaces would require additional regularization (e.g., eigenvalue clipping or shrinkage), introducing new hyperparameters and compromising the simplicity of the training-free paradigm.

## K Detailed Runtime Analysis

To provide a transparent account of the computational costs associated with different selection methods, we present a detailed breakdown of the wall-clock runtime in Table 13. All experiments were conducted on NVIDIA A100 80G GPU, and time was measured in hours.

The table decomposes the total pipeline duration into two key phases: **Data Selection** (the cost of the selection method itself) and **Visual Instruction**

**Tuning** (the cost of fine-tuning the model on the selected data subset).

- **Full-Finetune:** This serves as our baseline, requiring 94 GPU hours for tuning on the complete dataset, with zero selection cost.
- **TIVE:** This Training-Based method exemplifies the high overhead of existing approaches. The selection phase alone consumes 87 hours, which is 92% of the baseline’s entire tuning time. Although the final tuning is fast (14 hours), the total pipeline (101 hours) is 7.5% slower than simply fine-tuning on all data, resulting in an OSC score greater than 1.
- **PRISM:** Our method demonstrates exceptional efficiency. The entire selection process, including feature extraction and correlation computation, takes only 1.5 hours. This allows for a total pipeline time of just 29.5 hours, a **71% reduction** compared to the full fine-tuning baseline, robustly satisfying our efficiency principles.

Method	Data Selection	Visual Instruction Tuning	Overall
Full-Finetune	-	94 (Hours)	94
TIVE	87 (Hours)	14 (Hours)	101 ( <b>+7.5%</b> )
PRISM	1.5 (Hours)	28 (Hours)	29.5 ( <b>-71%</b> )

Table 13: Wall-clock runtime breakdown on an NVIDIA A100 80G GPU. All times are measured in hours. Percentages in the ‘Overall’ column indicate the change relative to the Full-Finetune baseline.